

# Simulating galactic outflows with kinetic supernova feedback

Claudio Dalla Vecchia<sup>1\*</sup> and Joop Schaye<sup>1†</sup>

<sup>1</sup>*Leiden Observatory, Leiden University, P.O. Box 9513, 2300 RA Leiden, the Netherlands*

22 February 2019

## ABSTRACT

Feedback from star formation is thought to play a key role in the formation and evolution of galaxies, but its implementation in cosmological simulations is currently hampered by a lack of numerical resolution. We present and test a sub-grid recipe to model feedback from massive stars in cosmological smoothed particle hydrodynamics simulations. The energy is distributed in kinetic form among the gas particles surrounding recently formed stars. The impact of the feedback is studied using a suite of high-resolution simulations of isolated disc galaxies embedded in dark halos with total mass  $10^{10}$  and  $10^{12} h^{-1} M_{\odot}$ . We focus in particular on the effect of pressure forces within the disc, which we turn off temporarily in some of our runs to mimic a recipe that has been widely used in the literature. We find that (ram) pressure forces on expanding superbubbles determine both the structure of the disc and the development of large-scale outflows. Pressure forces exerted by expanding superbubbles puff up the disc, giving the dwarf galaxy an irregular morphology and creating a galactic fountain in the massive galaxy. Hydrodynamic drag within the disc results in a strong increase of the effective mass loading of the wind for the dwarf galaxy, but quenches much of the outflow in the case of the high-mass galaxy.

**Key words:** methods: numerical — ISM: bubbles — ISM: jets and outflows — galaxies: evolution — galaxies: formation — galaxies: ISM

## 1 INTRODUCTION

Core-collapse supernovae (SNe) and winds from massive stars feed back energy into the interstellar medium (ISM). The energy released by massive stars can efficiently suppress subsequent star formation by destroying dense, star forming clouds, by generating supersonic turbulence and, if the star formation density is sufficiently high for individual supernova remnants to overlap, by blowing gas out of the disc. In starburst galaxies feedback from star formation may result in the development of a galaxy-wide superwind which may (temporarily) remove a large fraction of the gas, while in galaxies with less intense star formation feedback may lead to the development of a galactic fountain. Because these feedback mechanisms operate on time scales that are very short compared to the age of the universe, they can lead to self-regulation.

Feedback from star formation is thought to be a crucial ingredient for models of the formation and evolution of galaxies. Without it, star formation becomes much more efficient than observed, particularly in low-mass

galaxies (e.g. White & Frenk 1991). Among other things, galactic winds are also thought to be responsible for the enrichment of the intergalactic medium with heavy elements (e.g. Aguirre et al. 2001) and for pre-heating the gas that ends up in groups and clusters of galaxies (e.g. Ponman, Cannon, & Navarro 1999).

Modelling SN feedback in simulations of the formation of galaxies is known to be a difficult task, mostly because the injected thermal energy tends to be radiated away well before it has any hydrodynamical effect (e.g. Katz, Weinberg, & Hernquist 1996; Balogh et al. 2001). This overcooling problem is probably caused by the fact that current state-of-the-art simulations still lack the resolution to capture the physics of the multiphase ISM (e.g. Ceverino & Klypin 2007).

A typical SN ejects  $\sim 1 M_{\odot}$  at  $\sim 10^4 \text{ km s}^{-1}$ , which corresponds to a kinetic energy  $\sim 10^{51} \text{ erg}$ . Since the sound-crossing time is initially much smaller than the radiative cooling time, the remnant starts out as an adiabatic blast wave. Once radiative losses become important, the energy-conserving blast wave gives way to a momentum conserving snow-plough phase, whose deceleration is determined mostly by the amount of mass that is swept up by the wind. The initial phases in the evolution of a

\* E-mail: caius@strw.leidenuniv.nl

† E-mail: schaye@strw.leidenuniv.nl

superbubble driven by multiple SNe are very similar to the evolution of an individual SN remnant. However, if a superbubble blows out of the disc, its subsequent evolution may be strongly affected by the ram pressure of infalling gas and the gravitational attraction of the galaxy (e.g. Silich & Tenorio-Tagle 1998; Mac Low & Ferrara 1999; D’Ercole & Brighenti 1999; Silich & Tenorio-Tagle 2001; Fujita et al. 2004; Dubois & Teyssier 2008).

Current simulations lack the resolution to resolve individual SNe or, in the case of cosmological simulations<sup>1</sup> even superbubbles. The energy released by dying stars in a single resolution element per time step is typically distributed over a mass that exceeds the mass of SN ejecta by many orders of magnitude. The initial expansion velocity and post-shock temperature are therefore underestimated by large factors. Since the radiative cooling time scales as  $t_c \propto T^{1/2}$  above 1 keV, this implies that the cooling time is greatly underestimated. Because the injection radius is also far too large, the initial cooling time tends to be smaller than the bubble sound-crossing time. Thus, the simulation will skip the adiabatic blast-wave phase and the energy will typically be radiated away before a significant fraction of the thermal energy has been converted into kinetic energy.

The fact that poor resolution results in inefficient thermal feedback is generally attributed to a lack of spatial resolution: real SNe explode in hot bubbles of low-density gas, whereas the ISM in cosmological simulations consists of a single dense, “warm” phase. Mass resolution is, however, more fundamental. Without sufficient mass resolution, the first SNe will not be able to create a hot, low-density ISM phase in the first place.

Cosmological simulations must resort to sub-grid recipes to solve the overcooling problem.<sup>2</sup> Two types of solutions appear to work: injecting (part of) the SN energy in kinetic rather than thermal form (e.g. Navarro & White 1993; Mihos & Hernquist 1994; Kawata 2001; Kay et al. 2002; Springel & Hernquist 2003; Oppenheimer & Davé 2006; Dubois & Teyssier 2008) and/or suppressing radiative cooling by hand (e.g. Gerritsen 1997; Mori et al. 1997; Thacker & Couchman 2000; Kay et al. 2002; Sommer-Larsen, Götz, & Portinari 2003; Brook et al. 2004; Stinson et al. 2006). Although the suppression of cooling enables the efficient conversion of thermal energy to kinetic energy, the maximum wind velocity will still be underestimated if the total mass of the neighboring resolution elements exceeds that of a superbubble. Kinetic feedback can alleviate this problem by kicking only a small fraction of the resolution elements near the star particle. Kinetic feedback thus gives us the freedom to distribute a fixed amount of kinetic energy over a varying amount of mass. However, using this freedom to increase the initial wind velocity has the drawback that the imposed winds become more poorly sampled and therefore less isotropic. With increasing resolution, the two types of sub-grid

models for the generation of galactic winds are expected to converge.

A third approach, which is often combined with one of the above, is to employ a sub-grid model to describe the multiphase ISM (e.g. Yepes et al. 1997). Examples include imposing an effective equation of state which specifies the total pressure of the ISM as a function of its mean density (e.g. Springel & Hernquist 2003) and, at least for the case of smoothed particle hydrodynamics (SPH) simulations, using different types of particles to represent different thermal phases (e.g. Marri & White 2003; Scannapieco et al. 2006). While galactic winds can in principle be triggered naturally if the latter method is used, this again requires ad-hoc solutions in the absence of sufficient resolution.

To prevent the overcooling problem, simulations that impose an effective equation of state for the ISM must either make it extremely stiff, resulting in discs that are much thicker and smoother than observed, or employ a sub-grid recipe for galactic winds. However, even if it does not directly generate winds, the use of an effective equation of state for dense gas can be considered a necessary ingredient for simulations that lack the resolution and/or physics to model the multiphase ISM. If the equation of state is not modified by hand, gas will accumulate at unrealistically low temperatures and high densities in the absence of resolved feedback processes. As we discussed in Schaye & Dalla Vecchia (2008), using a power-law equation of state with a polytropic index of 4/3 has the advantage of yielding a Jeans mass that is independent of the density which makes it possible to suppress spurious fragmentation due to a lack of resolution.

It is, however, important to note that maintaining an effective equation of state in the presence of radiative losses would, in reality, require energy. The amount of energy that is required depends on unresolved physical processes and can therefore not be reliably determined. Imposing an equation of state for dense gas therefore implies that the energy available for any wind sub-grid model must be less than the energy provided by star formation.

The most widely used recipe for galactic winds in SPH simulations is the kinetic feedback model implemented by Springel & Hernquist (2003) (hereafter SH03). Motivated by the desire to impose the net mass loading and velocity of the wind after it has escaped from the disc and by the wish to make the recipe insensitive to numerical resolution, hydrodynamical forces on the wind particles are temporarily switched off in the SH03 model. Thus, winds cannot blow bubbles in the disc, drive turbulence or create channels in gas with densities typical of the ISM. Their sole effect on the disc is the removal of fuel for star formation by the ejection of wind particles.

Another aspect of the SH03 recipe is that wind particles are selected stochastically from all the dense (i.e. star-forming) particles in the simulation and are therefore not constrained to be neighbors of newly-formed stars. While this non-local feedback solves some numerical problems, we will argue that it can lead to undesirable behavior in galaxies that do not contain large numbers of particles (i.e. most galaxies in cosmological simulations), particularly if metal enrichment is included.

We present and test a modified variation of the SH03 recipe in which the winds are local and not decoupled hy-

<sup>1</sup> By cosmological simulations we mean simulations that model the evolution of a representative volume of the universe, as opposed to simulations that zoom in on one or a few galaxies.

<sup>2</sup> In the absence of efficient feedback mechanisms, the amount of cold gas predicted by cosmological simulations is limited by resolution. Hence, it is possible to roughly match the observed amount of cold gas at a particular redshift by tuning the resolution.

hydrodynamically. In this paper we will focus on the effects of hydrodynamical drag within the ISM. Using high-resolution SPH simulations of isolated disc galaxies we show that pressure forces exerted by and on wind particles have a dramatic effect on both the structure of the ISM and the development of galactic winds. Hydrodynamical drag on wind particles converts low-mass disc galaxies into irregulars and results in a strong increase of the net wind mass loading, while for high-mass galaxies it leads to the creation of bubbles and the development of a galactic fountain. Pressure forces within the disc reduce the kinetic energy in the wind above the disc by orders of magnitude.

This paper is organized as follows. We present our recipe for galactic winds and its implementation in SPH simulations in section 2. After describing our simulations of isolated disc galaxies in section 3, we present the results on the galaxies' morphology, star formation histories and large-scale winds in sections 4.1 to 4.3, respectively. In section 4.4 we present resolution tests which show that the effects of hydrodynamical drag are underestimated if the Jeans scale is unresolved. Finally, we summarize and discuss our conclusions in section 5.

## 2 KINETIC FEEDBACK IMPLEMENTATION

Following Aguirre et al. (2001) and SH03, we specify the kinetic feedback through two parameters: the initial mass loading and wind velocity. It is convenient to introduce a dimensionless wind mass loading parameter  $\eta$  by expressing the initial wind mass loading  $\dot{M}_w$  in units of the star formation rate  $\dot{M}_*$ ,

$$\dot{M}_w \equiv \eta \dot{M}_*. \quad (1)$$

Assuming that core-collapse SNe inject a kinetic energy of  $\epsilon_{\text{SN}}$  per solar mass of stars formed, the fraction of this energy carried by the wind is

$$f_w = \frac{\eta v_w^2}{2\epsilon_{\text{SN}}} \quad (2)$$

$$\approx 0.4 \left(\frac{\eta}{2}\right) \left(\frac{v_w}{600 \text{ km s}^{-1}}\right)^2 \left(\frac{\epsilon_{\text{SN}}}{1.8 \times 10^{49} \text{ erg M}_{\odot}^{-1}}\right)^{-1} \quad (3)$$

where  $v_w$  is the input wind velocity. The value  $\epsilon_{\text{SN}} \approx 1.8 \times 10^{49} \text{ erg M}_{\odot}^{-1}$  is appropriate for a Chabrier (2003) initial mass function (IMF) and a stellar mass range  $0.1\text{--}100 \text{ M}_{\odot}$  if all stars in the mass range  $6\text{--}100 \text{ M}_{\odot}$  end their lives as core-collapse SNe. For comparison, assuming a Salpeter (1955) IMF would yield  $\epsilon_{\text{SN}} \approx 1.1 \times 10^{49} \text{ erg M}_{\odot}^{-1}$ . We will use  $\eta = 2$  and  $v_w = 600 \text{ km s}^{-1}$  as our fiducial values, which implies that the winds carry about forty percent of the energy produced by core collapse SNe. The remainder is implicitly assumed to be lost radiatively.

These values are consistent with observations of local starburst galaxies, for which  $v_w$  increases with galaxy mass (or star formation rate) from tens to  $\sim 10^3 \text{ km s}^{-1}$ , while the mass in cold, outflowing gas ranges from  $\eta \sim 0.01$  to 10 (e.g. Veilleux, Cecil, & Bland-Hawthorn 2005, and references therein), and with redshift  $z \sim 3$  starburst galaxies, which typically have wind velocities of hundreds to  $\sim 10^3 \text{ km s}^{-1}$  (e.g. Shapley et al. 2003). Comparisons with observed values are, however, plagued by the fact that they apply only to certain gas phases and that it is not clear on

what scale they are measured. Moreover, it is not clear a priori how the wind mass loading and velocity predicted by the simulation correspond to the input values. In fact, studying this question is one of the main motivations for the present work.

Our recipe for kinetic feedback in SPH simulations is as follows. Once a star particle reaches an age  $t_{\text{SN}} = 3 \times 10^7 \text{ yr}$ , corresponding to the maximum lifetime of stars that end their lives as core-collapse SNe, it is allowed to inject kinetic energy into its surroundings by kicking one or more of its neighbors. We will refer to particles that have received a kick in the time interval  $[t - t_w, t]$ , where  $t$  is the current time, as wind particles. New wind particles are selected stochastically from the neighbouring gas particles of each newly-formed star particle. That is, each neighbouring gas particle has a probability

$$\text{Prob} = \eta \frac{m_*}{\sum_{i=1}^{N_{\text{ngb}}} m_{g,i}} \quad (4)$$

of becoming a wind particle, where  $m_*$  is the mass of the new star particle,  $m_{g,i}$  the mass of gas particle  $i$ ,  $N_{\text{ngb}}$  the number of neighbours within the SPH smoothing kernel ( $N_{\text{ngb}} = 48$  in our simulations), and the sum is over all gas particle neighbours that are not wind particles. The wind velocity is then added to the velocity of the wind particle with a random direction.<sup>3</sup>

The small time delay  $t_{\text{SN}}$  is unimportant for the simulations presented here, but we implemented it because it is physically sensible: it takes  $t_{\text{SN}}$  for the feedback energy to be released. We note that it may be important for simulations that follow the ejection of heavy elements by massive stars as a function of time because it prevents gas particles from being kicked before they are enriched.

The parameter  $t_w$  determines how long a gas particle that is kicked will remain classified as a wind particle. We do not allow wind particles to be kicked. This ensures that the wind velocity does not become much greater than  $v_w$ , which would not only complicate the interpretation of the simulations, but could also result in extremely small time steps. We also do not allow wind particles to be converted to star particles, in order to prevent the formation of spurious high velocity star particles. We set  $t_w = 1.5 \times 10^7 \text{ yr}$ , but note that similar or smaller values (including  $t_w = 0$ ) give nearly identical results.

It is clear that for  $\eta > N_{\text{ngb}}$ , and potentially for lower values of  $\eta$  in regions of intense star formation, and/or for large values of  $t_w$ , it can happen that all the gaseous neighbors of a newly-formed star particle are wind particles. For our default parameter values this problem is, in fact, negligible. However, to avoid a break down of the method for extreme parameter values, we keep track of the desired and actual global, cumulative mass in wind particles. If the actual mass falls below the desired mass (i.e. below  $\eta M_*$ , where  $M_*$  is the total stellar mass in the simulation), additional wind particles are selected stochastically from all star-forming particles that are not currently wind particles. Thus, this correction to the mass loading is a non-local form

<sup>3</sup> We implemented the possibility of giving the wind velocity the direction of the vector pointing from the star to the wind particle, but found no noticeable effects.

of kinetic feedback, much as is done for all wind particles in SH03. We stress the fact that this correction to the mass loading is negligible (i.e.  $\lesssim 1\%$ ) for all simulations presented here.

### 3 SIMULATIONS

We ran simulations of disc galaxies embedded in dark matter halos with total masses of  $10^{10}$  and  $10^{12} h^{-1} M_{\odot}$  (we use  $h = 0.73$ ). Runs were repeated using varying physical and numerical parameters. In this section we will briefly describe the code, the initial conditions and the runs we performed. We note that the code and initial conditions are identical to those used in Schaye & Dalla Vecchia (2008).

#### 3.1 Code and initial conditions

We use a modified version of the TreePM/SPH code GADGET (Springel, Yoshida, & White 2001; Springel 2005) for all the simulations presented in this paper.

We employ the star formation recipe of Schaye & Dalla Vecchia (2008), to which we refer the reader for details. Briefly, gas with densities exceeding the critical density for the onset of the thermo-gravitational instability ( $n_{\text{H}} \sim 10^{-2} - 10^{-1} \text{ cm}^{-3}$ ) is expected to be multiphase and star-forming (Schaye 2004). We therefore impose an effective equation of state with pressure  $P \propto \rho_g^{\gamma_{\text{eff}}}$  for densities exceeding  $n_{\text{H}} = 0.1 \text{ cm}^{-3}$ , normalized to  $P/k = 10^3 \text{ cm}^{-3} \text{ K}$  at the threshold. We use  $\gamma_{\text{eff}} = 4/3$  for which both the Jeans mass and the ratio of the Jeans length and the SPH kernel are independent of the density, thus preventing spurious fragmentation due to a lack of numerical resolution.

The Kennicutt-Schmidt star formation law is analytically converted and implemented as a pressure law. As we demonstrated in Schaye & Dalla Vecchia (2008), our method allows us to reproduce arbitrary input star formation laws for any equation of state without tuning any parameters. All the simulations presented here produce similar local Kennicutt-Schmidt laws, which implies that comparisons of the predicted star formation laws with observations cannot discriminate between different wind models. We use the observed Kennicutt (1998) law

$$\dot{\Sigma}_{*} = 1.5 \times 10^{-4} M_{\odot} \text{ yr}^{-1} \text{ kpc}^{-2} \left( \frac{\Sigma_g}{1 M_{\odot} \text{ pc}^{-2}} \right)^{1.4}, \quad (5)$$

where we divided Kennicutt's normalization by a factor 1.65 to account for the fact that it assumes a Salpeter IMF whereas we are using a Chabrier IMF.<sup>4</sup>

Radiative cooling and heating were included using tables for hydrogen and helium, assuming ionization equilibrium in the presence of the Haardt & Madau (2001) model for the  $z = 0$  UV background radiation from quasars and galaxies. The cooling tables were generated using the publicly available package CLOUDY (version 06.02; Ferland 2000).

The initial conditions were generated with a code

kindly provided to us by Volker Springel. Detailed descriptions of the model and its implementation are given in Springel, Di Matteo, & Hernquist (2005), so we will provide only a brief summary here.

The model consists of a dark matter halo, a stellar bulge, and an exponential disc of stars and gas. The circular velocities at the virial radii are 35.1 and 163  $\text{km s}^{-1}$  for the  $10^{10}$  and  $10^{12} h^{-1} M_{\odot}$  halos, respectively. The dark matter halo and the stellar bulge both follow Hernquist (1990) profiles scaled to match the inner density profile of a Navarro, Frenk, & White (1996) (hereafter NFW) profile with concentration  $c = 9$  and a mass within the virial radius equal to the total mass of the Hernquist profile. The equivalent NFW virial radii are then 35.1 and 163  $h^{-1} \text{ kpc}$  for the  $10^{10}$  and  $10^{12} h^{-1} M_{\odot}$  halos, respectively. The halo has a dimensionless spin parameter  $\lambda = 0.33$ . The disc contains 4 percent of both the total mass and the total angular momentum. The bulge contains 1.4 percent of the total mass and has a scale length one tenth of that of the disc. The bulge has no net rotation, while the dark matter halo and disc have the same specific angular momentum. The initial gas fraction of the disc is 30 percent, the remaining 70 percent of the disc mass is made up of stars. The vertical distribution of the stellar disc follows the profile of an isothermal sheet with a constant scale height set to 10 percent of the radial disc scale length. The vertical gas distribution is set up in hydrostatic equilibrium using an iterative procedure.

Except for our low-resolution runs, the total number of particles in each simulation is 4,800,736, of which 225,437 are gas particles in the disc. The baryonic particle mass for the  $10^{12} h^{-1} M_{\odot}$  halo is  $m_b = 5.1 \times 10^4 h^{-1} M_{\odot}$ . As discussed in Schaye & Dalla Vecchia (2008), this particle mass implies, for star-forming gas, a constant ratio of the total mass within a smoothing kernel to the Jeans mass,  $N_{\text{ngb}} m_b / M_J = 1/6$ , and a constant ratio of the kernel to the Jeans length  $h/L_J = 1/(48)^{1/3}$ . Although the  $10^{10} h^{-1} M_{\odot}$  halo requires a factor 100 less particles to resolve the Jeans scales by the same margin, we choose to use the same number of particles as for the  $10^{12} h^{-1} M_{\odot}$  halo in order to achieve a similar sampling of the outflows. The dark matter particle mass is higher than that for baryonic particles by a factor  $(\Omega_m - \Omega_b)/\Omega_b \approx 4.6$ .

The gravitational softening length was set to  $\epsilon_b = 10 h^{-1} \text{ pc}$  for the baryons and to  $(m_{\text{dm}}/m_b)^{1/3} \epsilon_b \approx 17 h^{-1} \text{ pc}$  for the dark matter. This is sufficiently small to resolve the Jeans length by at least two softening lengths up to gas surface densities of  $\sim 10^{4.5-5} M_{\odot} \text{ pc}^{-2}$ , which greatly exceed the central surface density for both halos.

#### 3.2 Runs

Table 1 lists all 16 simulation runs we have performed. Each simulation was evolved for 500 Myr. Our fiducial simulations are labelled *m10* and *m12* for the  $10^{10}$  and the  $10^{12} h^{-1} M_{\odot}$  halos, respectively. These runs used the recipe for galactic winds described in section 2, with mass loading  $\eta = 2$  and wind velocity  $v_w = 600 \text{ km s}^{-1}$ . In addition, we carried out the following variations:

- One run without galactic winds (*m[10,12]nowind*).
- Two runs with the same input wind energy as the fiducial model, but with  $(\eta, v_w) = (1, 848 \text{ km s}^{-1})$

<sup>4</sup> Note that we assumed a Salpeter IMF in Schaye & Dalla Vecchia (2008).



**Table 1.** Simulation parameters: total mass,  $M$ ; input mass loading,  $\eta$ ; input wind velocity,  $v_w$ ; total number of particles,  $N_{\text{tot}}$ ; total number of gas particles in the disc,  $N_{\text{disc}}$ ; mass of baryonic particles,  $m_b$ ; mass of dark matter particles,  $m_{\text{DM}}$ ; gravitational softening of baryonic particles,  $\epsilon_b$ ; gravitational softening of dark matter particles,  $\epsilon_{\text{DM}}$ ; wind feedback included, (Wind); wind particles hydrodynamically decoupled, (Decoupled). Values different from the fiducial ones are shown in bold.

Simulation	$M_{\text{halo}}$ ( $h^{-1} M_{\odot}$ )	$\eta$	$v_w$ ( $\text{km s}^{-1}$ )	$N_{\text{tot}}$	$N_{\text{disc}}$	$m_b$ ( $h^{-1} M_{\odot}$ )	$m_{\text{DM}}$ ( $h^{-1} M_{\odot}$ )	$\epsilon_b$ ( $h^{-1} \text{pc}$ )	$\epsilon_{\text{DM}}$ ( $h^{-1} \text{pc}$ )	Wind	Decoupled
<i>m10</i>	$10^{10}$	2	600	5000 494	235 294	$5.1 \times 10^2$	$2.4 \times 10^3$	10	17	Y	N
<i>m10nowind</i>	$10^{10}$	–	–	5000 494	235 294	$5.1 \times 10^2$	$2.4 \times 10^3$	10	17	<b>N</b>	–
<i>m10<math>\eta</math>1v848</i>	$10^{10}$	<b>1</b>	<b>848</b>	5000 494	235 294	$5.1 \times 10^2$	$2.4 \times 10^3$	10	17	Y	N
<i>m10<math>\eta</math>4v424</i>	$10^{10}$	<b>4</b>	<b>424</b>	5000 494	235 294	$5.1 \times 10^2$	$2.4 \times 10^3$	10	17	Y	N
<i>m10dec</i>	$10^{10}$	2	600	5000 494	235 294	$5.1 \times 10^2$	$2.4 \times 10^3$	10	17	Y	<b>Y</b>
<i>m10lr008</i>	$10^{10}$	2	600	<b>625 061</b>	<b>29 411</b>	$4.1 \times 10^3$	$1.9 \times 10^4$	<b>20</b>	<b>34</b>	Y	N
<i>m10lr064</i>	$10^{10}$	2	600	<b>78 132</b>	<b>3 676</b>	$3.3 \times 10^4$	$1.5 \times 10^5$	<b>40</b>	<b>68</b>	Y	N
<i>m10lr512</i>	$10^{10}$	2	600	<b>9 766</b>	<b>459</b>	$2.6 \times 10^5$	$1.2 \times 10^6$	<b>80</b>	<b>136</b>	Y	N
<i>m12</i>	$10^{12}$	2	600	5000 494	235 294	$5.1 \times 10^4$	$2.4 \times 10^5$	10	17	Y	N
<i>m12nowind</i>	$10^{12}$	–	–	5000 494	235 294	$5.1 \times 10^4$	$2.4 \times 10^5$	10	17	<b>N</b>	–
<i>m12<math>\eta</math>1v848</i>	$10^{12}$	<b>1</b>	<b>848</b>	5000 494	235 294	$5.1 \times 10^4$	$2.4 \times 10^5$	10	17	Y	N
<i>m12<math>\eta</math>4v424</i>	$10^{12}$	<b>4</b>	<b>424</b>	5000 494	235 294	$5.1 \times 10^4$	$2.4 \times 10^5$	10	17	Y	N
<i>m12dec</i>	$10^{12}$	2	600	5000 494	235 294	$5.1 \times 10^4$	$2.4 \times 10^5$	10	17	Y	<b>Y</b>
<i>m12lr008</i>	$10^{12}$	2	600	<b>625 061</b>	<b>29 411</b>	$4.1 \times 10^5$	$1.9 \times 10^6$	<b>20</b>	<b>34</b>	Y	N
<i>m12lr064</i>	$10^{12}$	2	600	<b>78 132</b>	<b>3 676</b>	$3.3 \times 10^6$	$1.5 \times 10^7$	<b>40</b>	<b>68</b>	Y	N
<i>m12lr512</i>	$10^{12}$	2	600	<b>9 766</b>	<b>459</b>	$2.6 \times 10^7$	$1.2 \times 10^8$	<b>80</b>	<b>136</b>	Y	N

and (4,424  $\text{kms}^{-1}$ ), respectively (*m*[10,12] $\eta$ 1v848 and *m*[10,12] $\eta$ 4v424);

- One run in which the wind particles are temporarily decoupled hydrodynamically (*m*[10,12]*dec*);
- Three runs in which the number of particles was decreased by factors of 8, 64 and 512, respectively (*m*[10,12]*lr*008, *m*[10,12]*lr*064, *m*[10,12]*lr*512)

In runs *m*[10,12]*dec* the wind particles are decoupled from the hydrodynamics in exactly the same manner as in SH03. That is, wind particles do not feel and do not contribute to the pressure forces for a time 50 Myr (corresponding to a distance of 31 kpc for a velocity of 600  $\text{km s}^{-1}$ ) or until their density has fallen below 10% of the threshold density for SF (i.e. until  $n_{\text{H}} < 10^{-2} \text{ cm}^{-3}$ ), whichever occurs first.

## 4 RESULTS

### 4.1 Morphology

Fig. 1 shows edge- and face-on projections of the gas density at time  $t = 250$  Myr for models *m10* (left-hand column), *m10nowind* (middle column) and *m10dec* (right-hand column). A comparison of the first two columns shows that the inclusion of a galactic wind has dramatic consequences for the morphology of the dwarf galaxy. The wind blows low-density bubbles in the disc, opening up channels through which it can escape into the halo. The outflowing wind particles drag large amounts of disc gas along, creating plumes of gas above and below the disc. The net result is a substantially puffing up of the galaxy, giving it a diffuse and irregular morphology, in good agreement with HI observations of nearby dwarf galaxies (e.g. Puche et al. 1992; Staveley-Smith et al. 1997; Kim et al. 1999; Stanimirovic et al. 1999; Walter & Brinks 1999). The

velocity field, which is indicated by the arrows in the edge on projections, shows that our recipe for galactic winds naturally produces a bi-conical outflow, with higher velocities near the minor axis.

In contrast, when the wind is hydrodynamically decoupled (right-hand column), the galaxy retains its initial morphology and the disc remains smooth and thin. Apart from a small decrease of the density due to the removal of mass in the form of the wind particles themselves, the only visible effect of the decoupled winds is that the disc has become smaller and thinner. This can be attributed to the fact that gas at large scale heights and/or large radii has a density sufficiently low for the wind particles to be recoupled hydrodynamically (recall that wind particles are recoupled when their density has fallen below 10 percent of the star formation threshold). Wind particles are therefore able to remove the lowest density gas in the disc but cannot replace it by dragging gas up from the inner parts of the galaxy because of the temporary decoupling. Because the outer most parts of the disc always have a low density, we find that the disc continues to shrink throughout the simulation. In terms of morphology, the model with decoupled winds closely resembles the run without galactic winds (middle column), except that the outer disc has been removed.

The outflow produced by the decoupled wind is isotropic rather than bipolar. The maximum outflow velocity is about 500  $\text{km s}^{-1}$ , about a factor of five greater than for our fiducial model *m10*. The higher velocities are also reflected in the temperature of the wind (not shown), which is more than an order of magnitude higher than that of *m10*.

As can be seen from the two left-most columns in Fig. 2, the effect of the wind on the morphology of our massive galaxy is less dramatic, though still significant. The edge-on projection shows that our recipe for galactic winds results in the creation of a clumpy halo. The clumps are in fact cold,

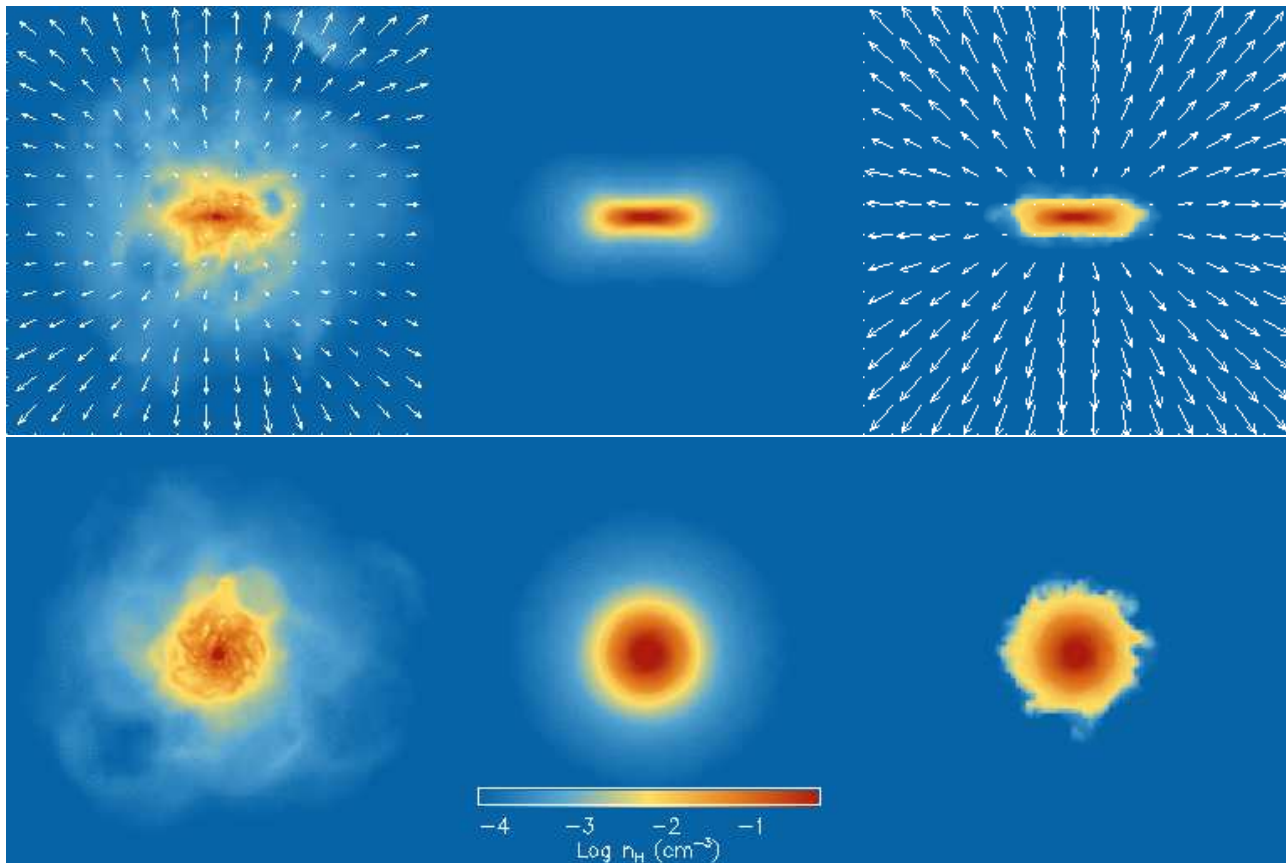


**Figure 1.** Edge- and face-on projections of the disc gas distributions for models *m10* (left-hand column), *m10nowind* (middle column), and *m10dec* (right-hand column) at time  $t = 250$  Myr. While the default galactic wind dramatically alters the morphology, the model using decoupled winds resembles the model without winds. Images are  $17.5 h^{-1} \text{ kpc}$  on a side and only show the gas component of the disc. The color coding is logarithmic in density. The color scale is fixed in each image and is indicated by the color bar in the lower middle panel. The maximum vector length corresponds to a velocity of  $106 \text{ km s}^{-1}$  for *m10* and  $502 \text{ km s}^{-1}$  for *m10dec*. The velocity field is not shown for model *m10nowind*.

infalling clouds that have been formed through thermal instabilities in the hot wind fluid. The clouds become more numerous and more prominent during the course of the simulation. While the outflow is initially fastest along the minor axis, by the end of the simulation the velocities are higher for gas flowing out at smaller angles with the disc, where the halo density is lower because less gas has been dumped there by the wind.

A comparison of the face-on projections indicates that the wind reduces the prominence of the spiral arms and suppresses their fragmentation. The wind not only enhances the stability of the disc, it also creates low-density bubbles and increases the size of the disc. The increase in the radial extension of the disc occurs partially because gas is pushed outwards by the wind and partially because gas blown out of the inner disc rains back at large distances.

As was the case for the low-mass galaxy, the morphology of the galaxy that uses hydrodynamically decoupled winds (right-hand column) looks most similar to the model without winds (middle column), except that the outer disc has been ejected. As we will show below, the reason why the density above and below the disc is lower than in our fiducial model is that the gas is moving through the halo with a much higher velocity. In contrast to the clumpy galactic fountain

produced by our fiducial run, the decoupled winds result in a smooth and isotropic outflow.

For videos showing the evolution of the gas density, temperature, and velocity field, we refer the reader to the web site <http://www.strw.leidenuniv.nl/DS08/>.

## 4.2 Star formation history

The need to reduce the efficiency of star formation forms the main motivation for the inclusion of sub-grid recipes for galactic winds in cosmological simulations. Before demonstrating that our method does indeed strongly suppress the total star formation rate (SFR), we note that thanks to our use of the sub-grid model for star formation presented in Schaye & Dalla Vecchia (2008), all of our models agree with the same local, Kennicutt-Schmidt star formation law.<sup>5</sup>

The left-hand panel of Fig. 3 shows the evolution of the SFR for all high-resolution runs of the low-mass galaxy. In the absence of galactic winds (dotted curve) the SFR

<sup>5</sup> The local Kennicutt-Schmidt laws predicted by models *m12* and *m12nowind* were shown by Schaye & Dalla Vecchia (2008), but using a Salpeter IMF rather than the Chabrier IMF used here.

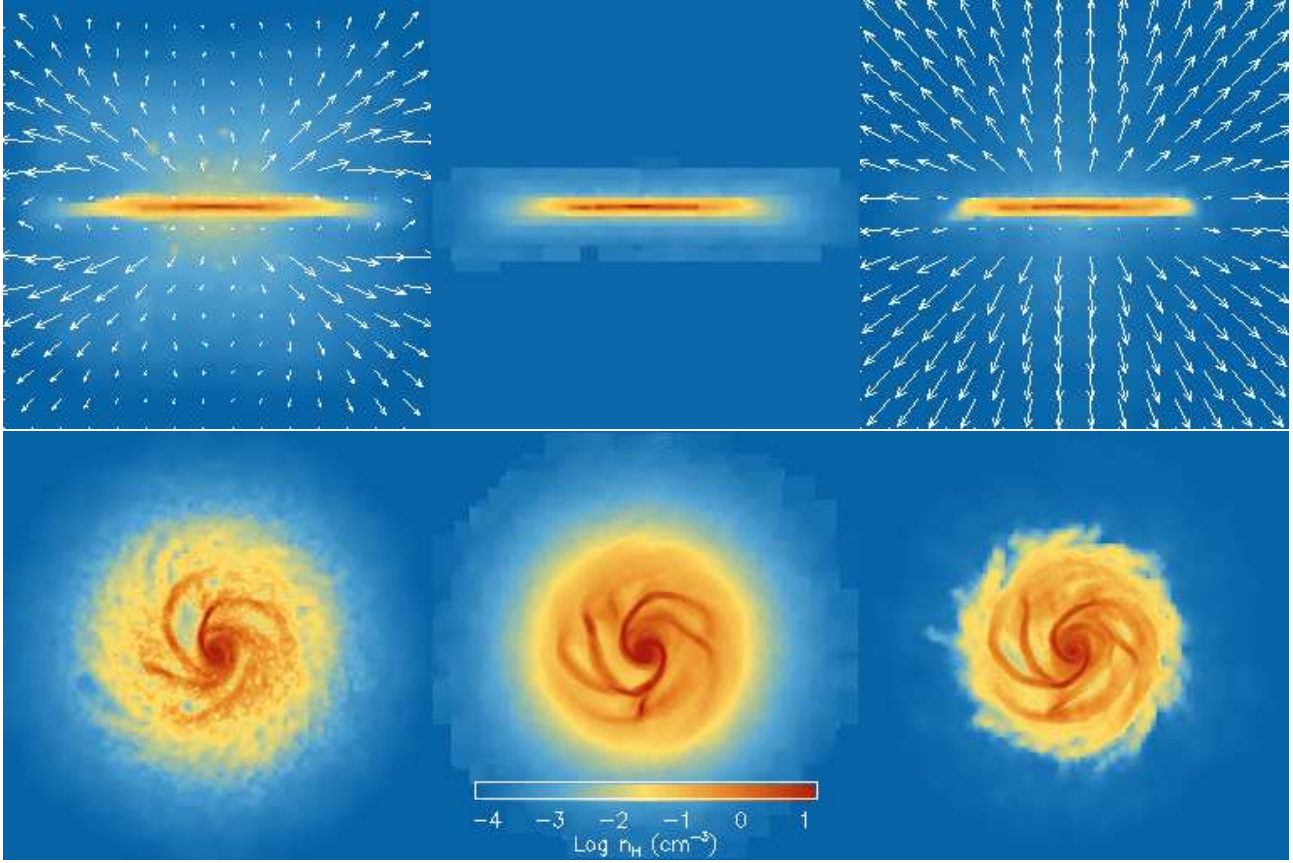


**Figure 2.** Edge- and face-on projections of the disc gas distributions for models *m12* (left-hand column), *m12nowind* (middle column), and *m12dec* (right-hand column) at time  $t = 250$  Myr. The default wind model produces a bi-conical outflow and results in a larger and more stable disc. Hydrodynamically decoupled winds produce a high-velocity wind, but have little impact on the morphology. Images are  $45 h^{-1}$  kpc on a side and only show the gas component of the disc. The color coding is logarithmic in density. The color scale is fixed in each image and is indicated by the color bar in the lower middle panel. The maximum vector length corresponds to a velocity of  $141 \text{ km s}^{-1}$  for *m12* and  $396 \text{ km s}^{-1}$  for *m12dec*.

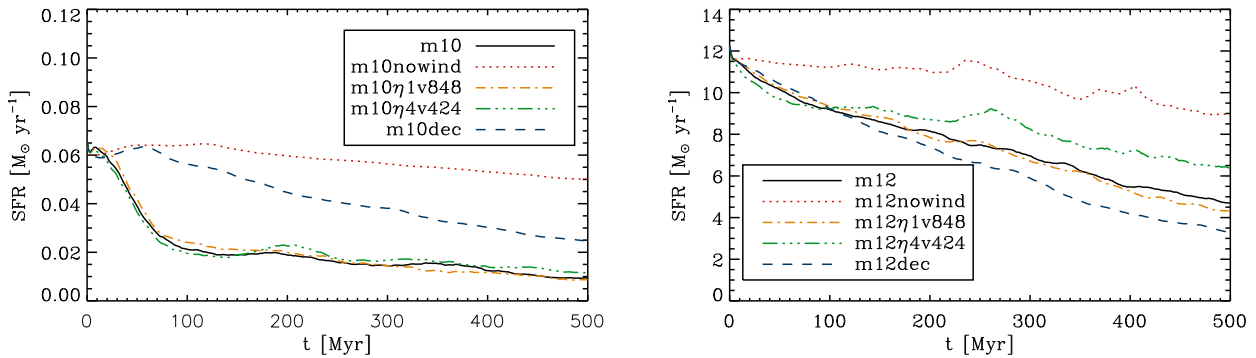


**Figure 3.** Star formation rate as a function of time for the  $10^{10}$  and  $10^{12} h^{-1} M_{\odot}$  galaxies (left-hand and right-hand panels, respectively). Galactic winds strongly reduce the star formation rate in all runs that include them. While hydrodynamically decoupling the winds reduces their impact on the star formation rate of the dwarf galaxy, the opposite is true for the massive galaxy. Variations of the mass loading and wind velocity while keeping the wind energy per unit stellar mass formed constant have no effect except for the lowest velocity in the massive galaxy.



decreases slowly due to gas consumption. For our fiducial model *m10* on the other hand (solid curve), the SFR initially decreases much more rapidly before transitioning to a more gradual decline after about 100 Myr. For most of the simulation the SFR is about a factor 6 lower than in model *m10nowind*. Varying the mass loading  $\eta$  and wind velocity  $v_w$  while keeping the input energy per unit stellar mass formed ( $\propto \eta v_w^2$ ) fixed has no significant effect on the SFR.

Decoupling the wind particles hydrodynamically (dashed curve) has a very large effect on efficiency of the feedback, yielding a SFR intermediate between those of models *m10* and *m10nowind*. The fact that the SFR for *m10* is much lower than that of model *m10dec* may indicate that hydrodynamical drag increases the effective mass loading to values that are greater than the input value.

Interestingly, the high-mass models (right-hand panel) show qualitatively different behavior. The winds still reduce the star formation in all runs, but this time the decrease is largest for the model with hydrodynamically decoupled winds (dashed curve). Apparently, many of the wind particles that can freely escape in model *m12dec* are stopped inside the disc due to pressure forces in the other runs.

Another difference with the low-mass galaxy is that the constant wind energy runs no longer give the same star formation histories. While the two highest wind velocity runs are still nearly the same, model *m12 $\eta$ 4 $v$ 424* has a significantly higher SFR. We conclude that models with a constant wind energy per unit stellar mass formed yield similar star formation histories provided that the wind velocity is above some minimum value. While this critical velocity must lie between 424 and 600 km s<sup>-1</sup> for the high-mass galaxy, it must be lower than 424 km s<sup>-1</sup> for the low-mass galaxy. The critical velocity therefore increases with galaxy mass and hence with the pressure of the ISM.

Note that when the winds are hydrodynamically decoupled, the SFR will generally depend on the choice of mass loading even for a fixed wind energy. In that case the sole effect of the winds is the removal of fuel for star formation and this happens at a rate that is determined by the choice of mass loading, provided the wind velocity is sufficiently high to overcome the gravitational attraction of the disc.

### 4.3 Mass outflow rate and wind velocity

Our sub-grid model for generating winds requires two parameters: the input mass loading  $\eta$  and the input wind velocity  $v_w$ . If the winds are hydrodynamically decoupled, then we expect the actual wind mass loading and velocity to be similar to the input values, at least when they are measured at radii small enough for gravitational deceleration to be unimportant. The situation could be quite different, however, when pressure forces in the disc are taken into account. In this section we will investigate this question by measuring the mass outflow and wind velocity as a function of time and radius.

The net mass outflow rate through a surface  $S$  is

$$\dot{M} = \int_S \rho \mathbf{v} \cdot d\mathbf{S}, \quad (6)$$

where  $\rho$  is the gas density and  $\mathbf{v}$  is the gas velocity relative to the origin, which we take to be the center of the galaxy.

The mass outflow can be split into outflow and inflow components according to the sign of the product  $\mathbf{v} \cdot \mathbf{r}$ . The net outflow rate is then the sum of these two components. We discretize the above equation as follows

$$\dot{M}(r, \Delta r) = \frac{1}{\Delta r} \sum_{i=1}^{N_{\text{shell}}} m_i \mathbf{v}_i \cdot \frac{\mathbf{r}_i}{r_i}, \quad (7)$$

where  $\Delta r$  is the thickness of a spherical shell of radius  $r$  centered on the origin (we use  $\Delta r = r_{\text{vir}}/150$ ) and  $N_{\text{shell}}$ ,  $m_i$  and  $\mathbf{r}_i$  are, respectively, the total number, mass and position of the particles that are within that shell.

The average outflow velocity is the mass-weighted radial velocity where only particles moving away from the origin (i.e.  $\mathbf{v}_i \cdot \mathbf{r}_i > 0$ ) are included:

$$\langle v \rangle = \frac{\sum_{i=1}^{N_{\text{shell}}} m_i (\mathbf{v}_i \cdot \frac{\mathbf{r}_i}{r_i})_+}{\sum_{i=1}^{N_{\text{shell}}} m_i}, \quad (8)$$

where the subscript  $+$  is used to indicate that only outgoing particles are taken into account.

#### 4.3.1 Models *m10* and *m10dec*

Fig. 4 shows the mass outflow rate (left-hand column) and the mean outflow velocity (right-hand column) for models *m10* and *m10dec*. The top row shows the time evolution measured at  $r = 0.2r_{\text{vir}}$ , while the bottom row illustrates the dependence on radius as measured at time  $t = 500$  Myr.

Let us start with the evolution of the mass flux (top-left panel). After a rapid, initial rise, the net mass outflow rate in model *m10* (solid curve) decreases smoothly with time. By the end of the simulation infall starts to become significant (dotted curve). Note that since there was no gaseous halo in the initial conditions, all of the infalling gas must have been blown out at earlier times. It is interesting to compare the net outflow rate with the input mass outflow rate  $\eta \dot{M}_*(t')$  (dot-dashed curve) which we evaluate at the retarded time  $t' = t - r/v_w$ . Clearly the net mass flux is much greater than the input value. This confirms that most wind particles drag many other gas particles along.

The dashed and dot-dot-dot-dashed curves correspond to the actual and input net mass loading for model *m10dec*. As expected, they agree much better than for model *m10*. When pressure forces are temporarily turned off, the wind particles can freely escape into the halo and there is no opportunity to change the wind mass loading. Even for this model the net mass loading slightly exceeds the input value, however, which implies that at the time when pressure forces are turned back on (i.e. when the density falls below one tenth of the star formation threshold) at least some wind particles are still in the outer layers of the disc and can therefore drag some other particles along. This also explains why the disc in model *m10dec* is somewhat smaller and thinner than in model *m10nowind* (see Fig. 1). The net mass outflow rate is, however, much smaller than for model *m10*, which explains why the hydrodynamically decoupled winds yield a much smaller reduction of the SFR than our fiducial wind model (see Fig. 3).

The top-right panel of Fig. 4 shows the evolution of the mean outflow velocity. After a sudden rise, the velocity drops to a steady value of slightly less than 50 km s<sup>-1</sup>, far



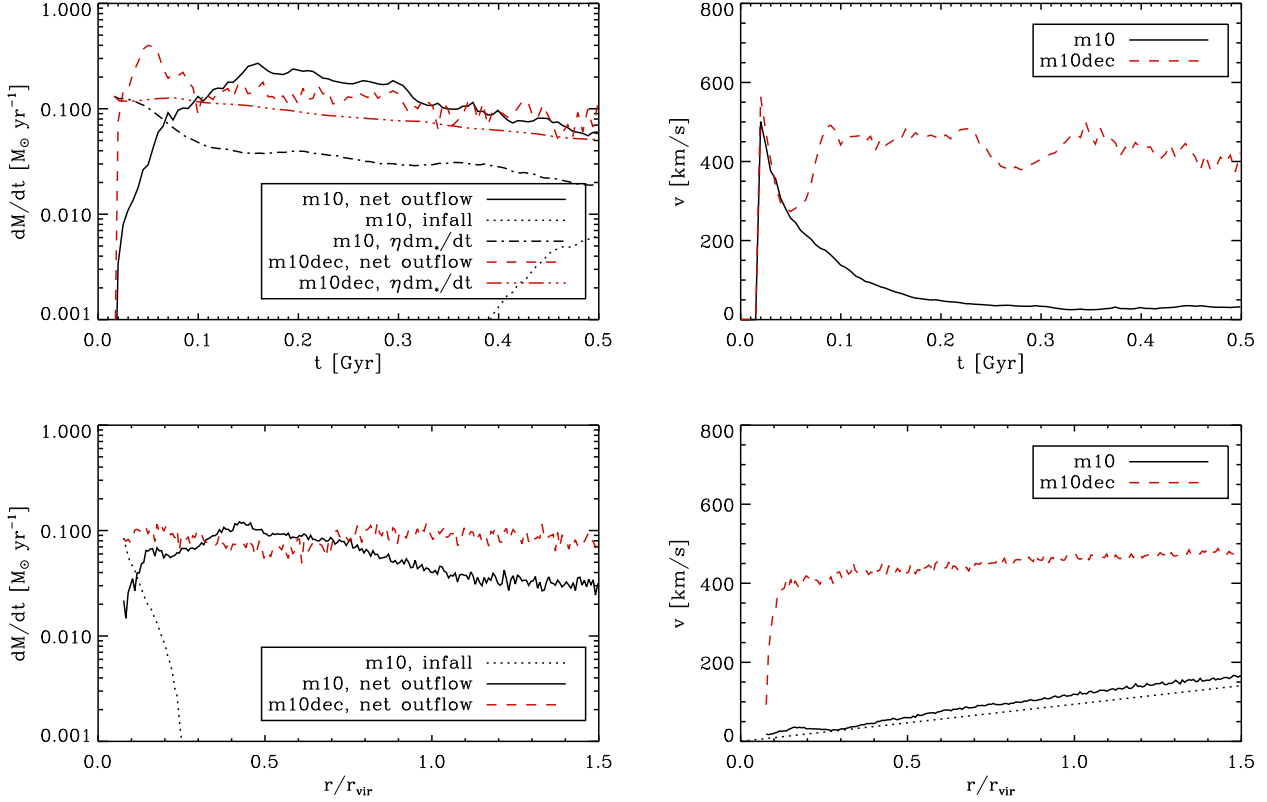


**Figure 4.** Mass outflow rate (left-hand column) and average outflow velocity (right-hand column) measured through a spherical shell at radius  $r = 0.2r_{\text{vir}}$  as a function of time (top row) and at  $t = 500$  Myr as a function of radius (bottom row) for models *m10* and *m10dec*. The dotted line in the bottom-right panel indicates the velocity required to reach the corresponding radius if the wind were launched from  $r = 0$  at time  $t = 0$ . All other curves are labelled in the legends. Model *m10* has a net mass outflow rate that strongly exceeds the input mass loading, whereas the two are similar for model *m10dec* in which wind particles temporarily do not feel pressure forces. Decoupling the wind particles from the hydrodynamics yields much greater outflow velocities.

below the input value of  $600 \text{ km s}^{-1}$ . We note, however, that there is significant scatter around this value and that some particles have much higher velocities, particularly around the minor axis (see Fig. 1). The mean outflow velocity is low because a typical wind particle has to penetrate the large amount of gas blown out at the beginning of the simulation before it can escape into the vacuum (see Fig. 1).

The mean outflow velocity in run *m10dec* is about  $400 \text{ km s}^{-1}$ , which exceeds that of *m10* by an order magnitude. The outflow velocity is smaller than the input value  $v_w = 600 \text{ km s}^{-1}$  because of projection effects and because some hydro drag is felt in the outer layers of the disc, not because of gravitational deceleration.

The outflow velocity in *m10* is in perfect agreement with observations of dwarf galaxies with similar circular velocities and star formation rates (Schwartz & Martin 2004). In contrast, outflow velocities as large as predicted by model *m10dec* have only been observed in galaxies that have star formation rates exceeding that of *m10dec* by two orders of magnitude (e.g. Rupke, Veilleux, & Sanders 2005; Martin 2005; Veilleux, Cecil, & Bland-Hawthorn 2005). This suggests that pressure forces within the disc are instrumental in shaping the winds emanating from dwarf galaxies.

The bottom row of Fig. 4 shows how the mass outflow rate and wind velocity vary with radius at time  $t = 500$  Myr,

which marks the end of the simulations. The net mass outflow rates (bottom-left panel) are nearly independent of radius. For model *m10* infall becomes significant at  $r < 0.2r_{\text{vir}}$  (dotted curve) but it is negligible at all radii for *m10dec* (not shown).

While the outflow velocity is nearly constant for model *m10dec* (bottom-right panel, dashed curve), it shows a strong increase with radius for model *m10* (solid curve). The dotted line indicates the velocity with which a particle needs to travel to reach the corresponding radius after 500 Myr. The actual outflow velocity can exceed this value if the gas was launched less than 500 Myr ago or it can fall below the dotted line if the wind has decelerated and/or if it was launched from radii greater than zero. Model *m10* roughly tracks the dotted line, which implies that the increase in the outflow velocity with radius is a trivial consequence of the combination of a relatively small outflow velocity and a finite time interval since the launch of the wind. In other words, for each radius the wind is close to the minimum value it must have in order to reach that radius. Note that a similar trend may well be present in real starburst galaxies, provided that they are observed within a few hundred million years after a sharp rise in their star formation rates.

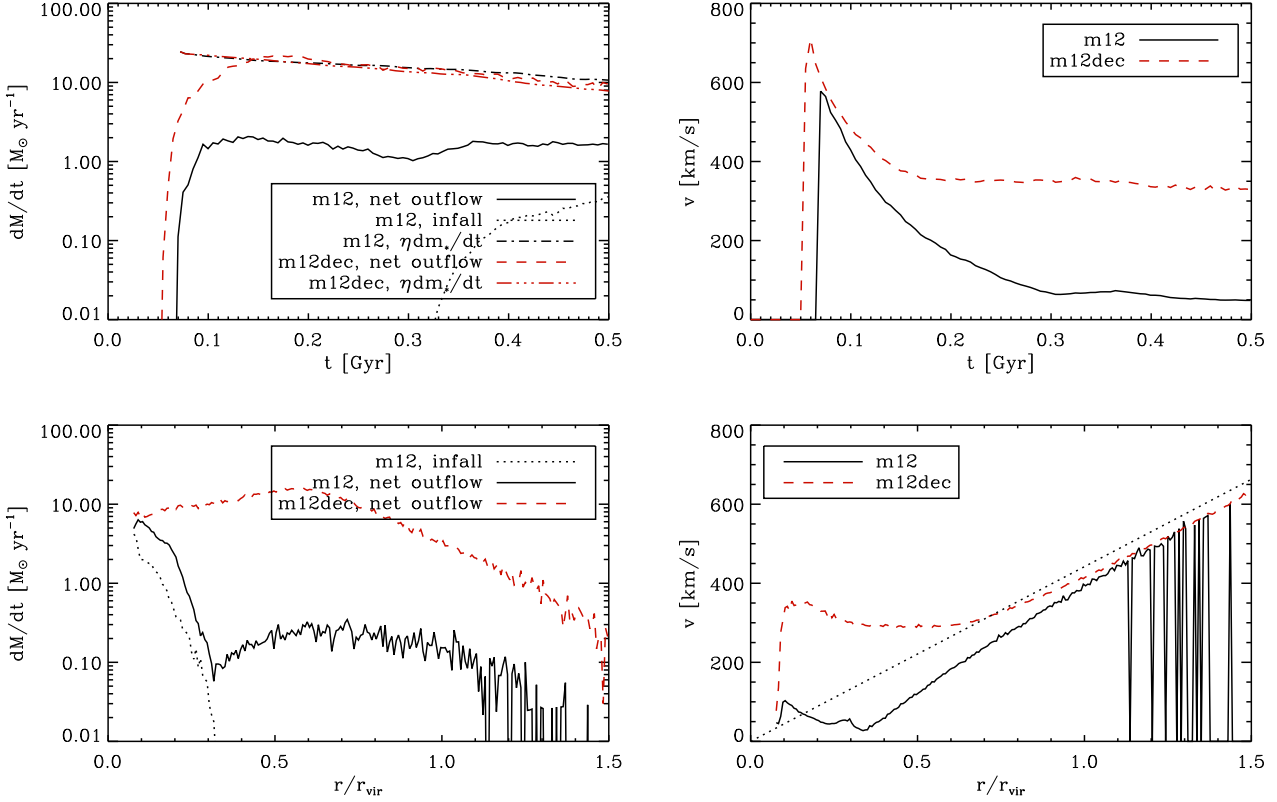


**Figure 5.** As Fig. 4 but for models *m12* and *m12dec*. Contrary to the result for *m10*, the net mass loading for model *m12* is much lower than the input value. When the winds are hydrodynamically decoupled, the actual value again agrees with the input value. Decoupling the wind particles from the hydrodynamics yields much greater outflow velocities. The radial dependence of the outflow velocities tracks the dotted line, which implies that the increase with radius is due to the finite time that has elapsed since the launch of the wind.

#### 4.3.2 Models *m12* and *m12dec*

Fig. 5 is identical to Fig. 4 except that it shows the results for the  $10^{12} h^{-1} M_\odot$  galaxy. While many of the results are qualitatively similar to those for the  $10^{10} h^{-1} M_\odot$  galaxy, there are also some noticeable differences. The most important difference is that the net mass outflow for model *m12* is an order of magnitude below the input value (top-left panel, solid and dot-dashed curves), whereas it exceeded the input value in the case of *m10* (see Fig. 4). Apparently, most of the wind particles are halted by pressure forces before they can escape the disc of the massive galaxy.

In contrast, when pressure forces are temporarily switched off, the actual and input mass loading agree very well (dashed and dot-dot-dot-dashed curves). This explains why, for the massive galaxy, the decoupled winds are more effective at reducing the SFR than the winds in our default model and why the situation is reversed for the dwarf galaxy (see Fig. 3). The pressure of the ISM in dwarf galaxies is too low to quench the wind, allowing it to drag large amounts of gas out of the disc. In high-mass galaxies the ISM pressure must be greater in order to support the larger surface densities and the main effect of hydrodynamical drag is to stop the wind from escaping the disc.

We note, however, that the ability to completely quench the wind, i.e., to stop the wind particles before they have moved significantly, must depend on the ram pressure ex-

erted by individual wind particles and hence on the input wind velocity. Thus, models with identical input wind energies, but higher wind velocities may produce larger mass outflows for massive galaxies. Fig. 3 indicates that increasing the wind velocity from 600 to 848  $\text{km s}^{-1}$  for our  $10^{12} h^{-1} M_\odot$  galaxy does not make a difference, whereas decreasing it to 424  $\text{km s}^{-1}$  reduces the impact of the wind. This could be largely a numerical effect since the ram pressure exerted by individual wind particles depends on their mass. Fig. 3 demonstrates that once the input velocity is above some critical value, which increases with galaxy mass, the results become independent of the way in which the available wind energy is distributed.

The bottom-right panel of Fig. 5 illustrates other differences between the high- and low-mass galaxies. At a fixed fraction of the virial radius, the outflow velocities are higher than for the dwarf galaxy. Furthermore, for  $r \gtrsim r_{\text{vir}}$ , not only *m12* but also *m12dec* track the dotted line which indicates the radius that a wind particle launched with the corresponding velocity can reach within 500 Myr. All these differences can be explained by the fact that a fixed fraction of the virial radius corresponds to a greater physical radius for a more massive galaxy and that a higher velocity is required to reach a greater physical radius in a fixed amount of time.

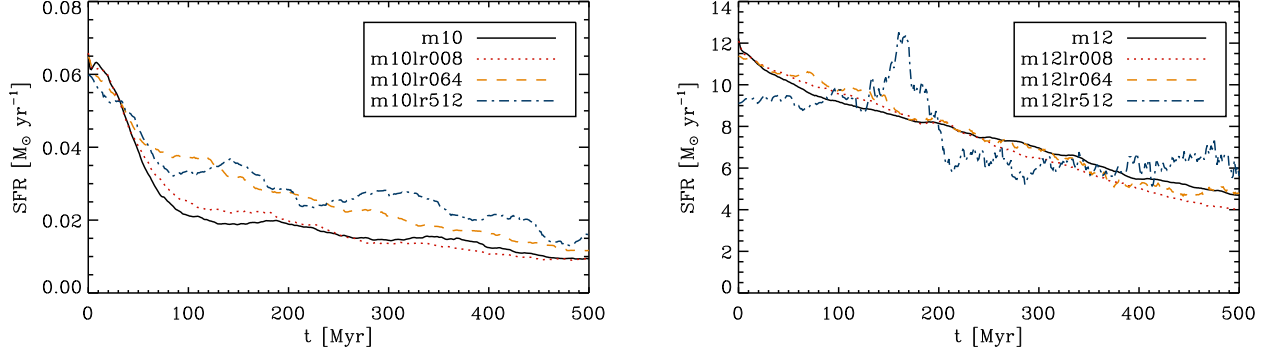


**Figure 6.** Resolution dependence of the star formation rate as a function of time for the  $10^{10}$  and  $10^{12} h^{-1} M_\odot$  galaxies (left-hand and right-hand panels, respectively). Resolution has only modest effects, except for model *m12lr512* which becomes violently unstable.

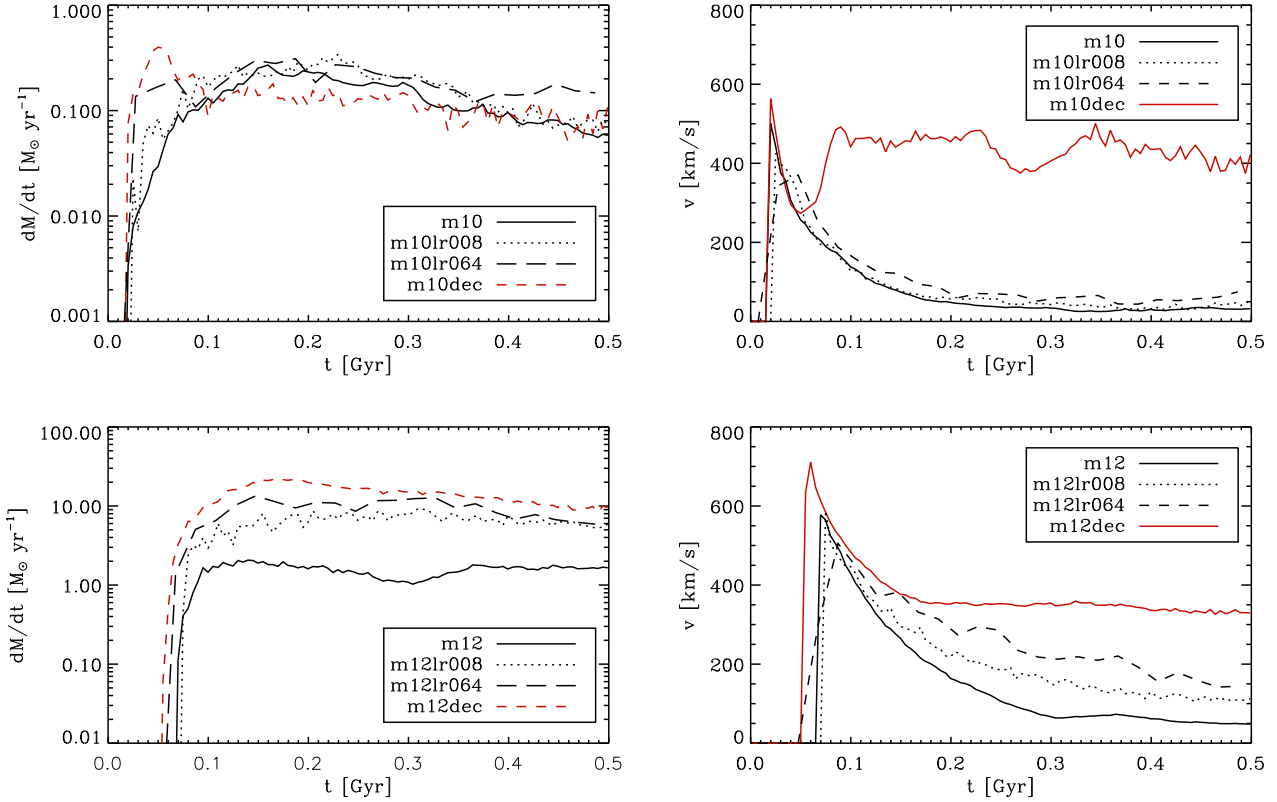


**Figure 7.** Resolution dependence of the mass outflow rate (left-hand column) and mean outflow velocity (right-hand column) measured through a spherical shell at radius  $r = 0.2r_{\text{vir}}$  as a function of time for the  $10^{10}$  (top row) and the  $10^{12} h^{-1} M_\odot$  (bottom row) galaxies. Decreasing the resolution yields higher mass outflow rates and higher outflow velocities for the high-mass galaxy, but has no discernible effect on the low-mass galaxy. Note that the particle mass in *m10lr064*, which is the lowest-resolution version plotted, is still lower than that in *m12*.

#### 4.4 Resolution tests

We performed resolution tests for our fiducial runs, decreasing the particle numbers by factors of 8, 64 and 512. Hence, the particle mass is increased by the same factors whereas the SPH smoothing kernels are increased by factors 2, 4 and 8, respectively (for a fixed density). Note that the lowest-resolution runs have only 459 particles in the disc and there-

fore do not provide enough samples to measure the wind properties.

As discussed in section 3.1, for star-forming gas in model *m12* the ratio of the kernel mass to the Jeans mass is  $1/6$  and the ratio of the kernel size to the Jeans length is  $1/(48)^{1/3}$  (recall that these ratios are constant because star-forming particles follow a power-law effective equation of state with polytropic index  $\gamma_{\text{eff}} = 4/3$ ). Hence, the Jeans scales are

not resolved by any of the lower resolution versions of the  $10^{12} h^{-1} M_{\odot}$  galaxy, whereas they are resolved by all but the *m10lr512* version of the  $10^{10} h^{-1} M_{\odot}$  galaxy.

Fig. 7 confirms that convergence requires resolving the Jeans scales. Interestingly, Fig. 6 demonstrates that high resolution is much less critical for obtaining a resolved SFR than it is for obtaining a converged estimate of the wind properties. This is probably due to the fact that the SFR is determined by the gas distribution in the disc, which is initially identical for all runs, whereas the wind is generated by the simulation itself. The situation would likely be quite different for an ab initio run using cosmological initial conditions. In such a simulation a galaxy consisting of only a few hundred particles would probably not even form a disc.

As the resolution is decreased, the net mass outflow rate and the wind velocity both increase for the high-mass galaxy. As expected, they remain the same for the low-mass galaxy. Thus, unresolved simulations give results that are more similar to the models in which the wind particles are temporarily decoupled hydrodynamically. However, even for the lowest resolution models for which we can still make meaningful measurements, the wind mass loading and outflow velocity are below those of model *m12dec*.<sup>6</sup>

The fact that decreasing the resolution mimics the effect of decoupling the hydrodynamics is not surprising. In the limit of only one particle per scale height, most wind particles will not encounter any other disc particles on their way out, leaving only the drag exerted by their original SPH neighbors.

## 5 SUMMARY AND DISCUSSION

Feedback from star formation is thought to play a key role in determining the observed properties of galaxies. It is therefore essential to include it in simulations of galaxy formation and evolution. Current simulations lack the resolution to resolve the energy conserving phase in the evolution of supernova remnants, causing any thermal energy input to be mostly radiated away before it has any significant hydrodynamical effect. Several types of sub-grid prescriptions for the generation of galactic winds have been proposed with the intent of overcoming numerical limitations. The most widely used methods use either thermal feedback combined with a temporary suppression of radiative cooling or kinetic feedback.

In this work we introduced a sub-grid recipe to model feedback from massive stars in cosmological SPH simulations. The energy is distributed in kinetic form among the neighbors of recently formed stars. We implemented our prescription in the SPH code GADGET and tested it using high-resolution simulations of isolated disc galaxies of total mass  $10^{10}$  and  $10^{12} h^{-1} M_{\odot}$ . Our kinetic feedback scheme strongly reduces the star formation rates and has a dramatic impact on the morphology of the galaxies.

The disc of the dwarf galaxy becomes puffed up and punctuated with low-density bubbles, resembling the HI observations of nearby galaxies. A bipolar outflow develops

naturally, with the largest velocities along the minor axis. The end result is a rather diffuse and irregular galaxy. Winds make the disc of the massive galaxy more stable, yielding more diffuse and less fragmented spiral arms. Its outer parts become more extended and also contain a large number of bubbles. While the wind is initially fastest along the minor axis, after a few hundred million years the velocities are higher at large opening angles because of strong infall along the minor axis. The infall is highly clumpy, consisting of cold gas clouds that have formed through thermal instabilities out of the hot wind.

The mean outflow velocity decreases with time, because gas that is blown out of the disc later must plough through gas that was blown out earlier, some of which has turned around and is falling back. At large radii the velocity increases with radius due to the fact that only gas with some minimum velocity can reach a given radius in the time since the initial starburst. The mean outflow velocities are much lower than the input values ( $600 \text{ km s}^{-1}$  for our fiducial model), except at the largest radii reached by the wind.

While the net mass outflow rate exceeds the input value ( $\dot{M}_w/\dot{M}_* = 2$  for our fiducial model) by about an order of magnitude for the dwarf galaxy, the reverse is true for the massive galaxy. Apparently, (ram) pressure forces in the disc enable the wind particles to drag large amounts of ISM out of the dwarf galaxy's disc, but are able to confine most wind particles to regions close to the disc in the case of the massive galaxy, whose ISM has both a higher density and pressure.

We varied the input wind velocity from 424 to  $848 \text{ km s}^{-1}$  while keeping the total kinetic energy per unit stellar mass formed constant by adjusting the input mass loading accordingly. For the dwarf galaxy the resulting star formation histories are all nearly identical and in the case of the massive galaxy only the lowest velocity run differed significantly. Thus, provided the input wind velocity is higher than some minimum value, which increases with the mass (and thus ISM pressure) of the galaxy, the results depend on the input kinetic energy but are insensitive to the amount of mass the energy is distributed over.

While the star formation histories are relatively insensitive to numerical resolution, convergence of the predictions for the outflows requires resolving the Jeans scale.

We contrasted our scheme with the sub-grid model of SH03 which has been widely used in the literature. In the SH03 prescription, the wind particles are selected stochastically from all the star-forming (i.e. dense) particles in the simulation and are therefore non-local. These wind particles are subsequently decoupled from the hydrodynamics for 50 Myr (i.e. 31 kpc if traveling at  $600 \text{ km s}^{-1}$ ) or until their density has fallen below 10 percent of the threshold for star formation.

In this work we have not tested the effects of non-locality because we expect them to be small for high-resolution simulations of individual galaxies such as those presented here. However, we do expect significant differences in cosmological simulations for which most galaxies will contain only a small number of star particles. In such galaxies the formation of star particles and the injection of kinetic energy will become essentially uncorrelated locally. To see this, note that for a galaxy that contains only a few star-forming particles, the typical time difference between the kicking of a wind particle and the creation of a star parti-

<sup>6</sup> If the wind particles are decoupled hydrodynamically, the results are nearly independent of resolution.



cle will be of order the gas consumption time scale divided by the input mass loading, or  $\sim 10^9/\eta$  yr at the threshold for star formation. This time scale greatly exceeds both the lifetime of massive stars and the simulation time step. The disconnection between the creation of a star particle and the injection of kinetic energy in its surroundings may have some undesirable consequences. For example, predictions for the chemical enrichment of the intergalactic medium may be affected because wind particles will contain an amount of heavy elements typical of particles in their host galaxies (which may often be zero) rather than abundances typical of the gas surrounding newly-formed stars.

We carried out simulations in which the wind particles were temporarily decoupled from the hydrodynamics as in the SH03 prescription. The difference between the predictions for the fiducial and decoupled models is dramatic. Decoupled winds have almost no effect on the morphology of the disc. Compared with the fiducial model and HI observations of nearby galaxies, the dwarf galaxy, which has a low enough surface density to be stable, is much smoother while the massive galaxy, which is unstable without the injection of turbulence, is more clumpy but lacks low-density bubbles. While the winds in the fiducial model slightly increase the size of the gas disc, the decoupled winds continuously shrink the disc. While the coupled winds drive a large-scale bipolar outflow from the dwarf galaxy and a clumpy galactic fountain in the massive galaxy, the decoupled winds produce isotropic outflows in both cases.

For the decoupled winds the outflow velocities (at least for  $r < r_{\text{vir}}$ ) are constant in time and nearly independent of the galaxy mass. The mean, projected outflow velocity is about 70 percent of the input value, which greatly exceeds the outflow velocities observed in starbursting dwarf galaxies. The net mass outflow rates are in good agreement with the input values. The kinetic energy in the wind escaping the disc is orders of magnitude higher than in the case of the coupled winds. Compared with the fiducial model, the decoupled winds are less efficient at suppressing the SFR in the dwarf galaxy, but more efficient for the massive galaxy. The wind properties in the decoupled runs are insensitive to numerical resolution, even when the Jeans scale is completely unresolved. The lower the resolution of the runs with coupled winds, the more they resemble the case of decoupled winds.

SH03 had several motivations for decoupling the winds hydrodynamically. They wanted to calibrate the sub-grid model with observations outside the disc, because they had no hope of resolving the structure of the ISM in their cosmological simulations, and they wanted a recipe that was insensitive to numerical resolution. Our tests clearly demonstrate that their method satisfies both these requirements.

One may question, however, whether the observational uncertainties are not far too large to enable a calibration of the wind velocity and mass loading outside the disc. It is currently not even clear how the observed values depend on radius and gas phase. It is also questionable whether it is desirable for the predictions of hydrodynamical simulations to be insensitive to resolution if the simulations do not resolve the Jeans scale.

Even if one is not interested in the internal structure of galaxies, which agrees less well with observations if the winds are decoupled, there are likely to be important differences

in other types of predictions. The fact that hydrodynamic drag makes low-mass galaxies much more diffuse may, for example, greatly affect predictions for quasar absorption line observations and may also alleviate the angular momentum problem (i.e. simulated discs are too small, probably due to excessive transfer of angular momentum to the dark matter halos). The fact that neglecting pressure forces on wind particles within the disc increases the kinetic energy of the escaping gas by very large factors, may have a large impact on predictions for the chemical enrichment of the intergalactic medium.

However, we stress that our simulations lack the resolution and the physics necessary to predict the structure of the multiphase ISM and to model the small-scale effects that ultimately lead to the development of galactic winds. We can therefore not exclude the possibility that future simulations will show the net effect of feedback from star formation to be more similar to that of decoupled winds. It is also important to note that while our artificial set-up of isolated, thin discs is useful for numerical experiments such as those presented here, it will exaggerate the differences between the coupled and decoupled winds. Galaxies in cosmological simulations are surrounded by gaseous halos and in the SH03 prescription wind particles will be re-coupled to the hydrodynamics before they leave the halos.

Summarizing, our results suggest that (ram) pressure forces in the disc and the inner halo have a very strong impact on the structure of the ISM and the properties of galactic winds. Pressure forces exerted by expanding superbubbles puff up disc galaxies, give low-mass starbursting galaxies irregular morphologies and stabilize the discs of massive galaxies. The energy lost in this process strongly reduces the kinetic energy carried by the outflowing gas. Even if the first bubbles open up a channel in the disc through which the gas can be efficiently ejected, it will run into the gas which was blown out earlier and has been decelerated in the process. For massive galaxies the reduction in the kinetic energy results in the development of a galactic fountain. When the resolution is too low to resolve the Jeans scale, the effects of hydrodynamic drag on the galactic winds will be underestimated.

## ACKNOWLEDGEMENTS

We are very grateful to Volker Springel for allowing us to use GADGET and his initial conditions code for the simulations presented here, as well as for useful discussions and help with his codes. We gratefully acknowledge discussions with the other members of the OWLS and Virgo collaborations. The simulations presented here were run on the Cosmology Machine at the Institute for Computational Cosmology in Durham as part of the Virgo Consortium research programme and on Stella, the LOFAR BlueGene/L system in Groningen. This work was supported by Marie Curie Excellence Grant MEXT-CT-2004-014112.

## REFERENCES

- Aguirre A., Hernquist L., Schaye J., Katz N., Weinberg D. H., Gardner J., 2001, *ApJ*, 561, 521

- Balogh M. L., Pearce F. R., Bower R. G., Kay S. T., 2001, MNRAS, 326, 1228
- Brook C. B., Kawata D., Gibson B. K., Flynn C., 2004, MNRAS, 349, 52
- Ceverino D., Klypin A., 2007, submitted to ApJ, arXiv:0712.3285
- Chabrier G., 2003, PASP, 115, 763
- D'Ercole A., Brighenti F., 1999, MNRAS, 309, 941
- Dubois Y., Teyssier R., 2008, A&A, 477, 79
- Ferland, G. J. 2000, Revista Mexicana de Astronomia y Astrofisica Conference Series, 9, 153
- Fujita A., Mac Low M.-M., Ferrara A., Meiksin A., 2004, ApJ, 613, 159
- Gerritsen J. P. E., 1997, PhD
- Haardt, F., & Madau, P. 2001, in the proceedings of XXXVI Rencontres de Moriond, astro-ph/0106018
- Hernquist L., 1990, ApJ, 356, 359
- Kawata D., 2001, ApJ, 558, 598
- Katz N., Weinberg D. H., Hernquist L., 1996, ApJS, 105, 19
- Kay S. T., Pearce F. R., Frenk C. S., Jenkins A., 2002, MNRAS, 330, 113
- Kennicutt R. C., Jr., 1998, ApJ, 498, 541
- Kim S., Dopita M. A., Staveley-Smith L., Bessell M. S., 1999, AJ, 118, 2797
- Mac Low M.-M., Ferrara A., 1999, ApJ, 513, 142
- Marri S., White S. D. M., 2003, MNRAS, 345, 561
- Martin C. L., 2005, ApJ, 621, 227
- Mihos J. C., Hernquist L., 1994, ApJ, 437, 611
- Mo H. J., Mao S., White S. D. M., 1998, MNRAS, 295, 319
- Mori M., Yoshii Y., Tsujimoto T., Nomoto K., 1997, ApJ, 478, L21
- Navarro J. F., White S. D. M., 1993, MNRAS, 265, 271
- Navarro J. F., Frenk C. S., White S. D. M., 1996, ApJ, 462, 563
- Oppenheimer B. D., Davé R., 2006, MNRAS, 373, 1265
- Ponman T. J., Cannon D. B., Navarro J. F., 1999, Natur, 397, 135
- Puche D., Westpfahl D., Brinks E., Roy J.-R., 1992, AJ, 103, 1841
- Rupke D. S., Veilleux S., Sanders D. B., 2005, ApJS, 160, 115
- Salpeter E. E., 1955, ApJ, 121, 161
- Scannapieco C., Tissera P. B., White S. D. M., Springel V., 2006, MNRAS, 371, 1125
- Schaye J., 2004, ApJ, 609, 667
- Schaye J., Dalla Vecchia C., 2008, MNRAS, 383, 1210
- Schwartz C. M., Martin C. L., 2004, ApJ, 610, 201
- Shapley A. E., Steidel C. C., Pettini M., Adelberger K. L., 2003, ApJ, 588, 65
- Silich S. A., Tenorio-Tagle G., 1998, MNRAS, 299, 249
- Silich S., Tenorio-Tagle G., 2001, ApJ, 552, 91
- Sommer-Larsen J., Götz M., Portinari L., 2003, ApJ, 596, 47
- Springel V., Yoshida N., White S. D. M., 2001, NewA, 6, 79
- Springel V., Hernquist L., 2003, MNRAS, 339, 289 (SH03)
- Springel V., 2005, MNRAS, 364, 1105
- Springel V., Di Matteo T., Hernquist L., 2005, MNRAS, 361, 776
- Stanimirovic S., Staveley-Smith L., Dickey J. M., Sault R. J., Snowden S. L., 1999, MNRAS, 302, 417
- Staveley-Smith L., Sault R. J., Hatzidimitriou D., Kesteven M. J., McConnell D., 1997, MNRAS, 289, 225
- Stinson G., Seth A., Katz N., Wadsley J., Governato F., Quinn T., 2006, MNRAS, 373, 1074
- Thacker R. J., Couchman H. M. P., 2000, ApJ, 545, 728
- Veilleux S., Cecil G., Bland-Hawthorn J., 2005, ARA&A, 43, 769
- Walter F., Brinks E., 1999, AJ, 118, 273
- White S. D. M., Frenk C. S., 1991, ApJ, 379, 52
- Yepes G., Kates R., Khokhlov A., Klypin A., 1997, MNRAS, 284, 235